Journal of Molecular Structure 1359 (2026) 145484

Contents lists available at ScienceDirect

Journal of Molecular Structure

journal homepage: www.elsevier.com/locate/molstr

Hydrogen-bonded supramolecular networks in hydrated nicotinoyl-hydrazones-based Derivatives with partial covalent character of O–H···N and O–H···O hydrogen bonds: Insights from X-ray and computational studies

Suman Adhikari [a,*], Ravichandran Deepa Roshini [b], Ghodrat Mahmoudi [c,d,*], Asmet N. Azizova [e,f], Olivier Blacque [g], M. Judith Percino [h], Subbiah Thamotharan [b,*]

[a] Department of Chemistry, Govt. Degree College, Dharmanagar, Tripura(N) 799253, India.
[b] Biomolecular Crystallography Laboratory, Department of Bioinformatics, School of Chemical and Biotechnology, SASTRA Deemed University, Thanjavur 613 401, India
[c] Department of Chemistry, Faculty of Science, University of Maragheh, P.O. Box 55136-83111, Maragheh, Iran.
[d] Department of Chemistry, Dogus University, Dudullu-Ümraniye, 34775 Istanbul, Türkiye.
[e] Azerbaijan Medical University, Scientific Research Centre (SRC), A. Kasumzade, St. 14. AZ 1022, Baku, Azerbaijan
[f] Scientific Research Center, Baku Engineering University, Khirdalan, Hasan Aliyev str. 120, AZ0101, Absheron, Azerbaijan
[g] Department of Chemistry, University of Zurich, Winterthurerstrasse 190, 8057 Zurich, Switzerland
[h] Unidad de Polímeros y Electrónica Orgánica, Instituto de Ciencias, Benemérita Universidad Autónoma de Puebla, Val3-Ecocampus Valsequillo, Puebla 72960, Mexico

ARTICLE INFO

Keywords:
Hydrogen-bonding networks
Hydrazone
Partial covalency
Hirshfeld surface analysis
QTAIM analysis
CLP-PIXEL

ABSTRACT

We report a comprehensive experimental and theoretical investigation of two hydrated nicotinoyl-hydrazone derivatives, (*E*)-*N*′-(1-(pyridine-4-yl)ethylidene)nicotinohydrazide dihydrate, **1·2H₂O** and (*E*)-*N*′-(1-(pyridine-4-yl)ethylidene)isonicotinohydrazide trihydrate **2·3H₂O**, focusing on their supramolecular organization, hydrogen-bonding networks, and electronic properties. Single-crystal X-ray diffraction discloses distinct hydration motifs and hydrogen-bond topologies arising from isomeric variation in the pyridyl substituent. Hirshfeld surface and 2D fingerprint analyses quantify contact contributions and highlight the roles of O–H···N, O–H···O, N–H···O, and C–H···O/N interactions in crystal packing. Enrichment analysis further reveals the most preferred interactions and the influence of the additional water molecule in compound **2**. Energy decomposition using CLP-PIXEL and DFT shows that water-mediated interactions are predominantly electrostatic, whereas dispersion governs weaker π-stacking contacts. QTAIM topological analysis identifies partial covalent character in key O–H···N and O–H···O hydrogen bonds, offering insight into their bonding nature and stability contributions. UV–Vis spectra supported by TD-DFT calculations further correlate electronic transitions with frontier orbital distributions. This integrated structural and computational study elucidates how hydration and isomerism modulate intermolecular interactions and material stability in molecular assemblies relevant to liquid-like and hydrogen-bonded systems.

1. Introduction

Various types of non-covalent interactions, including hydrogen bonding, π···π interaction, cation/anion···π interaction, chalcogen bonding, halogen bonding, pnictogen bonding, (an)agostic bonding, and tetrel bonding play essential roles across many areas of chemistry and biology [1–5]. Among these non-covalent contacts, hydrogen bonding and π···π contacts are arguably the most commonly recognized and extensively exploited to understand fundamental phenomena in chemistry and biology, predominantly in supramolecular chemistry and crystal engineering [6–8]. HB-driven self-assembly, characterized by directionality, specificity, reversibility, and strength, provides an effective strategy for constructing advanced supramolecular architectures [9]. Consequently, hydrogen bonding has become one of the most intensively studied topics in modern chemistry, owing to its crucial role in explaining and envisaging a wide range of phenomena across

* Corresponding authors.
E-mail addresses: sumanadhi@gmail.com (S. Adhikari), ghodratmahmoudi@gmail.com (G. Mahmoudi), thamu@scbt.sastra.edu (S. Thamotharan).

https://doi.org/10.1016/j.molstruc.2026.145484
Received 23 December 2025; Received in revised form 16 January 2026; Accepted 25 January 2026
Available online 26 January 2026

disciplines such as chemistry, biology, materials science, and environmental science [10–12]. In particular, supramolecular assemblies involving H-bonded water clusters continue to receive significant consideration because of their crucial contribution to the stability and functionality of biological systems [13,14].

Hydrazones derived from carbonyl compounds represent an important and multifaceted class of bioactive organic molecules, generally described by the structural motif $R_1R_2C{=}NNR_3R_4$ [15–17]. A defining feature of hydrazones, which distinguishes them from similar types of functional groups such as imines and oximes, is the existence of two interconnected N atoms. Compared to imines, hydrazones contain an additional amino-type N atom that enhances their coordination ability, along with an acidic N–H proton that enables intramolecular hydrogen bonding, anion sensing, and metal coordination [18,19]. The functional versatility of the azomethine moiety arises from its triatomic C=N−N framework, making hydrazones valuable in diverse applications, including medical chemistry. This unique structural feature significantly influences their chemical behaviour, particularly by increasing the nucleophilicity of the carbon atom within hydrazone-based scaffolds. The straightforward synthesis of hydrazones not only expands chemical diversity but also facilitates a deeper understanding of how lipophilic and hydrophobic properties influence molecular reactivity and functionality [20]. Considerable research has focused on their chelating ability, which allows hydrazones to form stable complexes with metal ions, thereby enhancing their applicability in coordination chemistry and contributing to their pharmacological relevance [21]. Hydrazones are also particularly attractive for crystal engineering and supramolecular chemistry because of their ease of synthesis, higher hydrolytic stability compared to imines, and inherent tendency to crystallize. Furthermore, nicotinoyl hydrazone-based derivatives are well suited for supramolecular assembly, as they can engage in π···π interactions through aromatic rings at both ends of the molecule and possess 3- or 4-pyridyl nitrogen atoms that act as effective hydrogen-bond acceptor sites [22].

In the present work, we report the synthesis and comprehensive characterization of two pyridyl isomers of nicotinoyl-hydrazone derivatives. Single-crystal X-ray diffraction, combined with theoretical approaches including CLP-PIXEL energy calculations, Hirshfeld surface analysis, quantum theory of atoms in molecule (QTAIM), and TD-DFT calculations, was employed to investigate the isomeric effects, intermolecular energetics, and the role of lattice water molecules in governing the supramolecular organization.

2. Experimental

2.1. Materials and physical measurements

All chemicals were of reagent grade, purchased from commercial suppliers, and used without further purification. FT-IR spectra were recorded using a Perkin-Elmer FT-IR spectrometer with KBr pellets over the range 4000-400 cm^{-1}. The ^1H NMR spectra in DMSO-d_6 were recorded with a Bruker Avance II 400 MHz spectrometer. The thermal stability of the samples was investigated using thermogravimetric analysis (TGA) on a Hitachi High-Tech Science STA200 instrument. The UV–vis spectrum was recorded on a Thermo Scientific EVOLUTION One UV-Vis Spectrophotometer.

2.2. Synthesis of the compounds 1 and 2

Scheme 1 outlines the synthetic route to compounds **1** and **2**. A solution of 3-pyridylcarbonyl hydrazine (0.5 g, 3.64 mmol) in ethanol (30 mL) was treated with 4-acetylpyridine (0.40 mL, 3.64 mmol), followed by the addition of five drops of glacial acetic acid. The reaction mixture was refluxed for 4 h, during which a white precipitate formed. The solid product was collected by filtration, purified by repeated washing with ethanol, and then air-dried. Single crystals of **1** suitable for X-ray diffraction were obtained from a saturated methanolic solution. The synthesis and crystallization of compound **2** followed an analogous procedure, except that 4-pyridylcarbonyl hydrazine was used in place of 3-pyridylcarbonyl hydrazine.

Powder X-ray diffraction (PXRD) measurements performed at room temperature confirmed the bulk phase purity of both compounds **1** and **2** (Figs. S1 and S2). The selected single crystals are representative of the bulk materials, as the experimental PXRD patterns closely match those simulated from the single-crystal structures using the Mercury 2024.1.0 program [23].

Compound **1**: Yield: 84%, ^1H NMR (400 MHz, $CDCl_3$, δ in ppm): 9.24 (brs, 1H), 9.16 (s, 1H), 8.78 (d, 1H), 8.65 (s, 2H), 8.25 (m, 1H), 7.48 (brs, 1H), 7.46 (m, 2H), 2.35 (s, 3H). FT-IR (ν cm^{-1}, KBr): 3416, 3176, 1681, 1590, 1409, 1279, 1151, 998, 898. M.p.: 174–176 °C.

Compound **2**: Yield: 86%, ^1H NMR (400 MHz, $CDCl_3$, δ in ppm): 9.07 (brs, 1H), 8.82 (s, 2H), 8.65 (s, 2H), 7.72 (d, 3H), 7.47 (brs, 1H), 2.45 (s, 3H). FT-IR (ν cm^{-1}, KBr): 3309, 3154, 3000, 1688, 1600, 1543, 1413, 1279, 1132, 998, 825. M.p.: 82–84 °C.

2.3. Single-crystal X-ray diffraction

Single crystal X-ray diffraction data for compounds **1** and **2** were collected at 160.0(1) K on a Rigaku OD Synergy/Hypix diffractometer using the Cu Kα radiation (λ = 1.54184 Å) from a dual wavelength X-ray

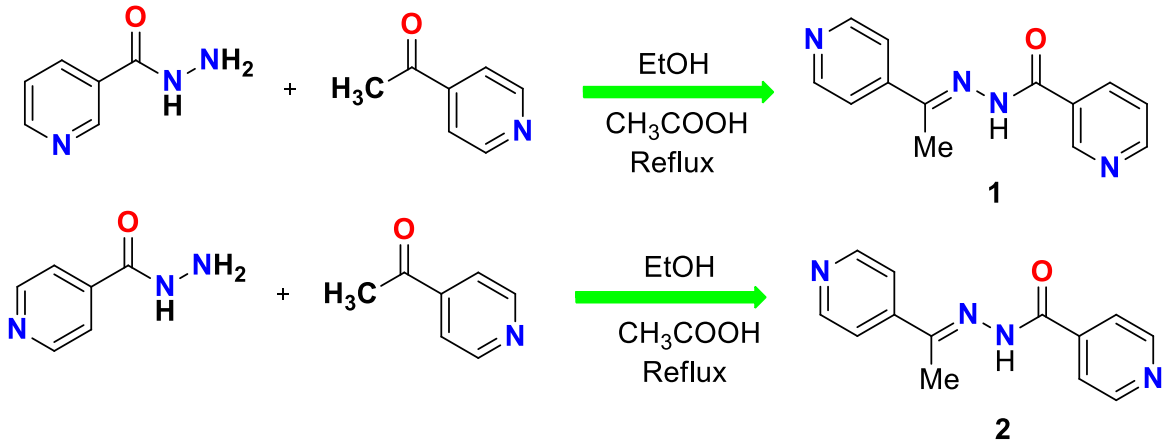

Scheme 1. Synthesis of the compounds **1** and **2**.

source and an Oxford Instruments Cryojet XL cooler. The selected suitable single crystal was mounted using polybutene oil on a flexible loop fixed on a goniometer head and immediately transferred to the diffractometer. Pre-experiment, data collection, data reduction and analytical absorption correction [24] were performed with the program suite *CrysAlisPro* (version 1.171.43.144a, Rigaku Oxford Diffraction Ltd, Yarnton, Oxfordshire, England, 2024). Using *Olex2* [25], the structure was solved with the *SHELXT* [26] small molecule structure solution program and refined with the *SHELXL* program package [27] by full-matrix least-squares minimization on F^2. The H-atoms attached to the O-atoms and N-atoms were located in a difference Fourier map, and were freely refined (position and isotropic displacement parameter). All remaining H-atoms were placed geometrically and refined isotropically using a riding model, with C—H = 0.95 Å (C-aromatic) and 0.98 Å (C-methyl), in association with U_{iso}(H) = 1.2U_{eq}(C-aromatic) or 1.5U_{eq}(C-methyl). *PLATON* [28] was used to validate the result of the X-ray analysis. Crystal data, data collection and structure refinement details are summarized in Table S1.

2.4. Computational details

All quantum chemical calculations were performed using the Gaussian09 program [29]. Prior to optimization, the C–H (1.083 Å), N–H (1.009 Å) and O–H (0.983 Å) bond distances were adjusted to typical neutron diffraction values [30]. Compounds **1** and **2** were first fully optimized (excluding lattice water molecules) using the B3LYP/6-311++G(d,p) level of theory, followed by vibrational frequency calculations. The gas-phase optimized structures were subsequently re-optimized in DMSO solvent using the CPCM solvation model at the same level of theory. Time-dependent (TD-DFT) calculations were then carried out to obtain the absorption spectra of both compounds.

Hirshfeld surface analyses were carried out using CrystalExplorer 21.5 [31]. Each fragment present in compounds **1** and **2** was analyzed independently. Intermolecular interaction energies for molecular dimers were evaluated using CLP-PIXEL energy analysis [32,33]. Since both compounds contain more than two molecular fragments and the CLP-PIXEL code can only process two fragments at a time, all possible pairwise combinations were considered. Electron densities were calculated at the MP2/6-31G** level of theory consistently with previously reported studies [34–37].

For comparison, intermolecular interaction energies of the molecular dimers were also calculated at the B97D3/def2-TZVP level of theory [38,39] using the counterpoise correction method [40]. Topological analysis of selected molecular dimers was carried out using the AIMALL program [41], based on wavefunctions obtained at the M06-2X-D3/def2-TZVP level of theory [42]. In addition, selected dimers were examined by noncovalent interaction (NCI) plot analysis [43], generated from wavefunctions computed at the same level of theory using Multiwfn-3.7 [44]. The NCI plots were visualized using the publicly available script at https://www.chi.ic.ac.uk/rzepa/cub2nci/.

3. Results and discussion

3.1. Spectral Characterization (FT-IR and NMR)

The FT-IR spectra of compounds **1** and **2** show strong absorption bands at 1681 and 1688 cm^{-1}, respectively, which are assigned to the ν(C=O) stretching vibrations (Figs. S3 and S4). Intense bands are detected at 1590 cm^{-1} for **1** and 1600 cm^{-1} for **2** correspond to the ν(C=N) stretching vibrations of the azomethine (-CH=N-) group, confirming the formation of hydrazones [45,46]. In addition, broad bands appearing in the regions 3416-3176 cm^{-1} for **1** and 3309 3143 cm^{-1} for **2** are attributed to ν(NH) and ν(H_2O) stretching vibrations.

The ^{1}H NMR spectra of compounds **1** and **2**, recorded in $CDCl_3$, are very similar. Each exhibits a broad singlet at 9.24 ppm for **1** and 9.07 ppm for **2**, corresponding to the -NH proton (Figs. S5 and S6). In both spectra, the -CH_3 protons were detected as singlets at 2.35 ppm for **1** and 2.45 ppm for **2**. The pyridyl ring protons of both compounds are observed in the aromatic region.

3.2. Structural description

Compound **1**, (*E*)-*N*′-(1-(pyridine-4-yl)ethylidene)isonicotinohydrazide, crystallizes in the triclinic system with two lattice water molecules and is denoted as **1.2H_2O**. In contrast, compound **2**, (*E*)-*N*′-(1-(pyridine-4-yl) ethylidene)nicotinohydrazide, crystallizes in the monoclinic system and incorporates three lattice water molecules, giving the formulation **2.3H_2O**. X-ray diffraction analysis shows that both compounds adopt an *E*-configuration around the C=N bond. Their molecular geometries are largely comparable, with no unusual structural features observed [37,47]. The key difference between them lies in the pyridyl ring attached to the C=O group: compound **1** contains a 4-pyridyl ring, whereas compound **2** features a 3-pyridyl ring. The ORTEP diagrams of the hydrated structures are presented in Fig. 1(a,b). A structural superimposition indicates that compounds **1** and **2** share a very similar overall conformation, particularly around their central molecular fragment (Fig. 1(c)). Only slight rotations of the terminal rings differentiate them. In both structures, the terminal rings are nearly coplanar, with dihedral angles of 3.88(2)° for **1.2H_2O** and 5.88 (3)° for **2.3H_2O**. The optimized structures of compounds **1** and **2** closely match their corresponding X-ray conformations. The bond lengths obtained from X-ray diffraction and DFT methods are comparable (Table S2). Superimposition analysis shows an excellent agreement between the experimental and optimized geometries, with only a slight rotation of the pyridyl rings observed, which can be attributed to crystal packing effects (Fig. 1(d, e)).

3.3. Hirshfeld surface and 2D fingerprint plots

Intermolecular interactions in the crystal packing of **1.2H_2O** and **2.3H_2O** were investigated using Hirshfeld surface (HS) analysis and the corresponding two-dimensional fingerprint plots (2D FP). HS analysis provides a clear visualization of hydrogen bonds and other close contacts that contribute to the stability of the crystal packing. Contacts shorter or longer than the sum of van der Waals radii appear on the surface as colour variations, ranging from red (shorter contacts) to white and blue (longer contacts). All Hirshfeld surfaces and fingerprint plots were generated using CrystalExplorer 21.5, as described in the experimental section.

For the **1.2H_2O** complex (Fig. 2), the HS of each component reveal the key intermolecular interactions. Molecule **1** shows intense red spots corresponding to N–H···O and O–H···N hydrogen bonds, along with broader, less intense red regions associated with O–H···N, O–H···O, and C–H···O interactions. The first lattice water molecule displays prominent red areas arising from O–H···N and O–H···O hydrogen bonds. The second lattice water molecule participates in three hydrogen bonds (O–H···N, N–H···O, and O–H···O). Together, these short and directional hydrogen bonds significantly contribute to the overall stability of the crystal packing.

The Hirshfeld surfaces of the **2.3H_2O** complex (Fig. 3) show similarities and differences compared to those of **1.2H_2O**. The common features include red spots near the NH and 4-pyridyl N atoms, corresponding to N–H···O and O–H···N hydrogen bonds. A key difference is observed at the amide C=O region: in **1.2H_2O** a red spot arises from a C–H···O interaction, whereas in **2.3H_2O** this region corresponds instead to an O–H···O hydrogen bond. The first lattice water molecule in the **2.3H_2O** crystal structure participates in O–H···O (intense red spots) and C–H···O (weaker spots) interactions but does not engage in O–H···N hydrogen bonding. The hydrogen-bonding pattern of the second lattice water molecule remains essentially unchanged between the two complexes. The third lattice water molecule in **2.3H_2O** forms O–H···N and O–H···O hydrogen bonds, again producing intense red spots on the surface. These short contacts play a key role in stabilizing the crystal

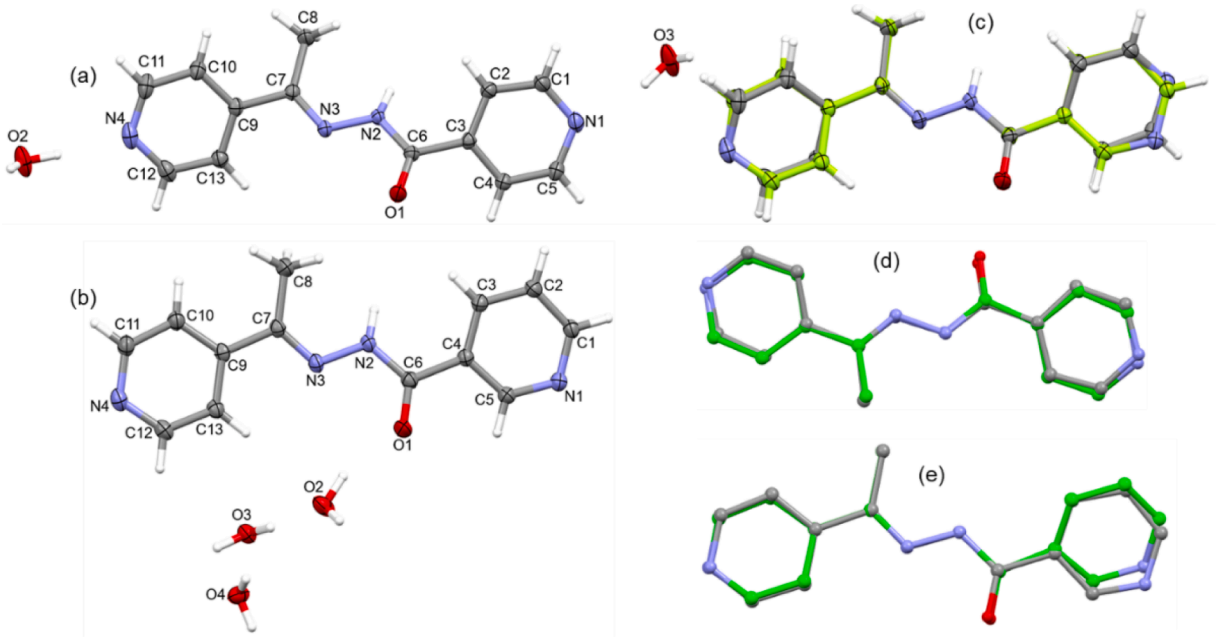

Fig. 1. ORTEP representations with atom-labelling schemes and ellipsoidal displacement at the 40% probability level for (a) **1.2H$_2$O**, (b) **2.3H$_2$O**, (c) superimposition of the X-ray conformations of **1** and **2**, (d) superimposition of the X-ray and optimized structures of **1**, and (e) superimposition of the X-ray and optimized structures of **2**.

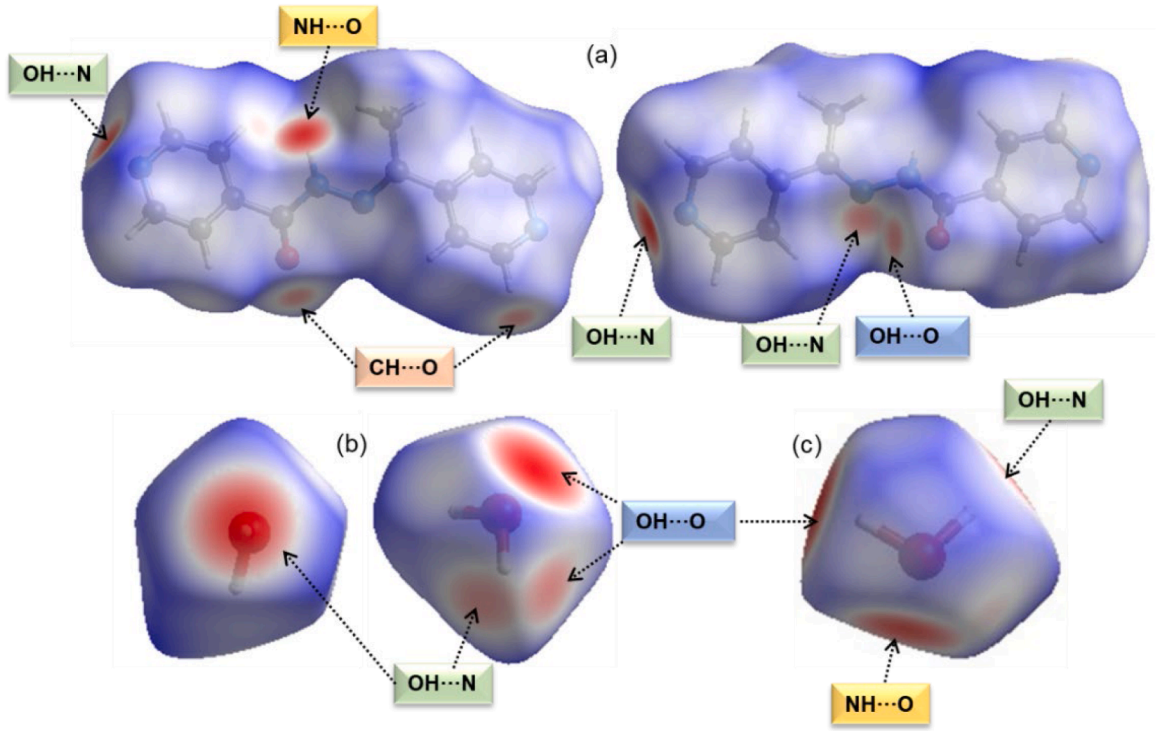

Fig. 2. Hirshfeld surfaces mapped over the normalized contact distance (d_{norm}) for (a) molecule **1** shown in two orientations, (b) the first lattice water molecule (O2) in two orientations, and (c) the second lattice water molecule (O3).

structure of **2.3H$_2$O**.

2D fingerprint plots highlight the individual intermolecular contact contributions to the crystal packing and help reveal both the isomeric effects and the influence of lattice water molecules (Fig. S7). In both **1** and **2**, H···H contacts make the largest contribution, with compound **2** showing an approximately 8% higher contribution, likely due to the presence of an additional lattice water molecule and isomeric effects. The H···O contacts, which account for O–H···O, N–H···O and C–H···O interactions, show comparable contributions in the two structures: 13.1% for **1** and 15.5% for **2**. The corresponding tip distances also differ slightly: 1.8 Å and 2.2 Å in **1** and 1.8 Å and 2.1 Å in **2**. A notable difference arises from the H···N contacts, representing O–H···N and C–H···N interactions. Compound **1** shows an 8.6% higher contribution, with tip distances at 1.8 Å (O–H···N) and 2.7 Å (C–H···N). In **2**, similar distances

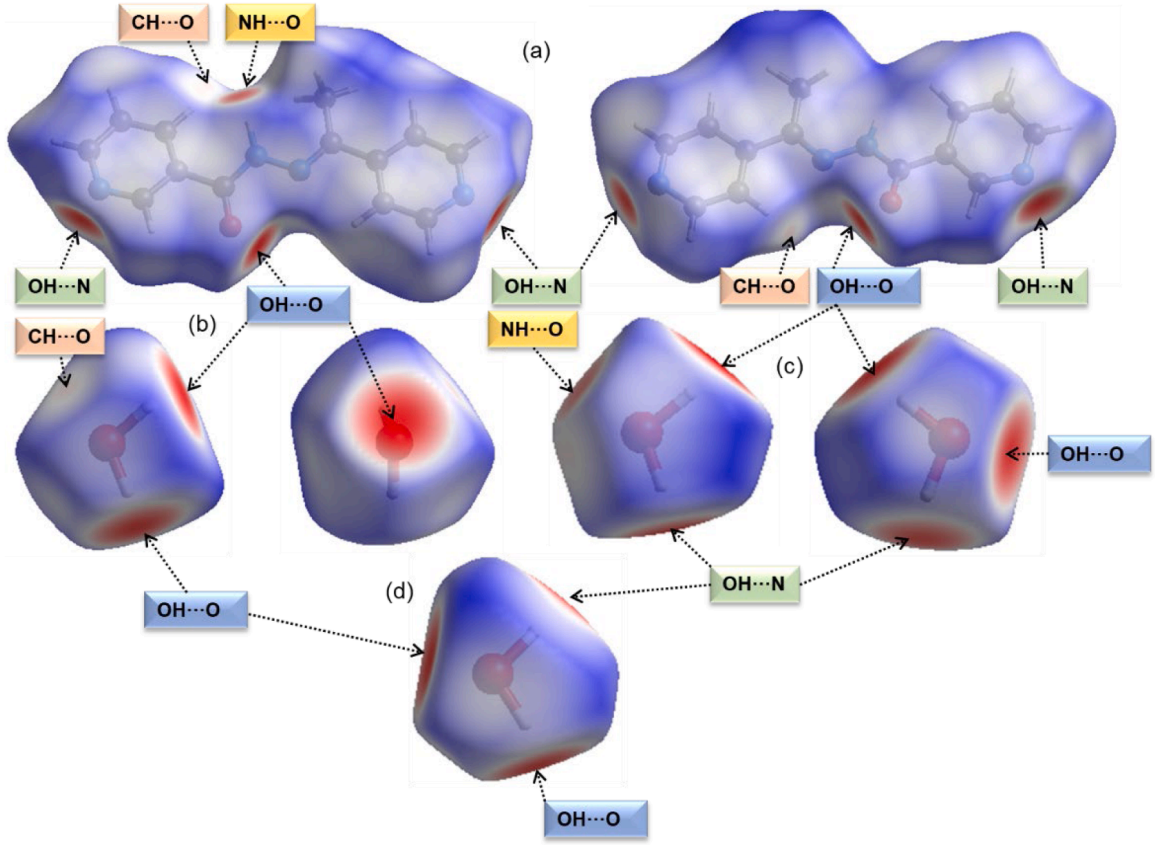

Fig. 3. Hirshfeld surfaces mapped over the normalized contact distance (d_{norm}) for (a) molecule **2** shown in two orientations, (b) the first lattice water molecule (O2) in two orientations, (c) the second lattice water molecule (O3) in two orientations, and (d) the third lattice water molecule (O4).

are observed at 1.8 Å and approximately 2.8 Å, though the upper tip is less scattered.

Differences are also observed in the contribution from π-stacking interactions, reflected in the C···C contacts, which amount to 6.4% in **1** and 9.5% in **2**. The cyan dots around 3.6 Å confirm the presence of stacking interactions, and the shape index maps show characteristic red-blue triangle pattern over the terminal rings, indicating participation in π-stacking (Fig. S8). Although H···C contacts, associated with potential C–H···π interactions, show notable contributions (16.4% in **1** and 9.1% in **2**) around 2.9 Å, no meaningful C–H···π interactions are actually observed. Other contacts contribute less and are unlikely to significantly influence the overall crystal stability.

The lattice water molecules were also examined individually in both structures (Fig. S9). In **1**, the first water molecule shows contribution of H···H (41.1%), H···O (36.3% and H···N (21.2%). The corresponding values in **2** are 45.9%, 41.3% and 11.0%, respectively, confirming that the water molecules participate in O–H···N, O–H···O and C–H···N interactions. In **2**, the first lattice water molecule is primarily involved in O–H···O, C–H···O contacts, as reflected by the high 58% contribution from H···O contacts. For the second lattice water molecule, the contributions of H···O (40.4%) and H···N (13.0%) indicate the formation of N–H···O, O–H···O and O–H···N hydrogen bonds. The third lattice water molecule shows contributions of H···O (38.6%) and H···N (11.7%), again confirming O–H···O and O–H···N hydrogen bonds. Overall, the lattice water molecules in both compounds significantly enhance crystal stability through diverse network of hydrogen bonds.

To support this assertion and quantitatively evaluate the influence of additional lattice water in compound **2**, we performed an enrichment ratio analysis of atomic contacts using the relative contributions of various intermolecular interactions derived from Hirshfeld surface analysis, as proposed by Jelsch et al. [48]. Enrichment ratios greater than unity indicate contacts that are favoured in the crystal packing. The Hirshfeld contact surfaces, random contacts, and enrichment ratios for compounds **1** and **2** are summarized in Table 1. For compound **1**, H···O, H···N, and C···C contacts exhibit enrichment ratios above unity, indicating that these interactions are the most favoured in its crystal structure. In contrast, compound **2** shows enrichment ratios greater than unity for H···H, H···O, N···N, C···N, and C···C contacts, highlighting a distinct redistribution of preferred intermolecular interactions. This shift clearly demonstrates the impact of the additional lattice water molecule in altering the dominant contacts in the solid state. Notably, H···H contacts become the most favoured in compound **2** due to the presence of the extra water molecule, while H···N contacts are no longer favoured. The increased enrichment of N···N and C···N contacts in **2** can be attributed primarily to enhanced molecular stacking in the crystal

Table 1
Hirshfeld contact surfaces, derived random contacts and enrichment ratios. The values in parentheses correspond to compound **2**.

Atoms	H	O	N	C
H	40.6 (48.6)			
O	15.5 (13.1)			
N	17.9 (9.3)	(1.0)	(2.6)	
C	16.4 (9.2)	0.5 (1.4)	2.7 (5.3)	6.4 (9.5)
Surface %	65.5 (64.4)	8.0 (7.8)	10.3 (10.4)	16.2 (17.4)
H	42.9 (41.5)	Random	Contacts	
O	10.5 (10.0)	0.6 (0.6)		
N	13.5 (13.4)	1.6 (1.6)	1.1 (1.1)	
C	21.2 (22.4)	2.6 (2.7)	3.3 (3.6)	2.6 (3.0)
H	0.9 (1.2)			Enrichment
O	1.5 (1.3)			
N	1.3 (0.7)	(0.6)	(2.4)	
C	0.8 (0.4)	0.2 (0.5)	0.8 (1.5)	2.5 (3.2)

lattice.

3.4. Supramolecular features of compound 1.2H_2O

In the crystalline state, molecules of **1** are arranged in parallel layers, with lattice water molecules positioned between these layers (Fig. 4(a)). To examine the supramolecular features and dimer energetics, CLP-PIXEL calculations were performed for three molecular pairs as detailed in the experimental section. The results are summarized in Table 2. Overall, the intermolecular interaction energies obtained from CLP-PIXEL agree well with those from DFT calculations.

The molecular pair consisting of molecule **1** and the first lattice water molecule (O2) generates nine molecular dimers. Of these, five dimers ($D1_A$–$D5_A$) arise between symmetry-related molecules of (*E*)-*N*′-(1-(pyridine-4-yl)ethylidene)isonicotinohydrazide, while four dimers ($D1_{AB}$–$D4_{AB}$) involve molecule **1** interacting with the lattice water. Dimer $D1_A$ is stabilized by π-stacking involving one of the 4-pyridyl rings, with a centroid–centroid distance of 3.657(7) Å. Dispersion energy accounts for 64% of its stabilization. Dimers $D2_A$ and $D5_A$ are supported by C–H···N interactions (Fig. 4(b)), where the hydrazide N3 and pyridyl N1 atoms act as acceptors. These interactions bridge molecules across different layers, and the overall supramolecular arrangement is further strengthened by π-stacking between adjacent layers (dimer $D4_A$, centroid–centroid distance 3.689(7) Å; 78% dispersion).

The $D2_A$ motif generates a $C(6)$ chain, whereas the $D5_A$ motif forms an $R_2^2(6)$ ring. $D2_A$ is predominantly dispersion-driven (78%), while stabilization of $D5_A$ arises from comparable contributions of electrostatic (53%) and dispersion (47%) energies. Dimer $D3_A$, stabilized by C–H···O interactions involving the amide oxygen, forms an $R_2^2(18)$ ring motif, with electrostatic energy contributing 65% to its stabilization. Adjacent D3A dimers are interconnected by the $D5_A$ motif (Fig. 4(c)), and similarly, connections are also established through the $D1_A$ motif (Fig. 4(d)).

As noted above, the first lattice water molecule (O2) forms four dimers with molecule **1**. Dimer $D1_{AB}$ is stabilized by an O–H···N interaction with a pyridyl nitrogen as observed in a closely related structure 4-benzoylpyridine isonicotinoyl hydrazone monohydrate [49], whereas $D2_{AB}$ features bifurcated O–H···N and O–H···O hydrogen bonds, generating an $R_1^2(5)$ motif. Together, these dimers link adjacent molecules of **1** into a loop forming an $R_4^4(18)$ motif represented in Fig. 5(a). The remaining water-mediated dimers ($D3_{AB}$ and $D4_{AB}$) are stabilized through C–H···O interactions. Combinations of $D2_{AB}$, $D3_{AB}$, and $D5_A$ further build the supramolecular assembly depicted in Fig. 5(b). Another architecture arises from the cooperative involvement of $D2_{AB}$, $D3_{AB}$, $D4_{AB}$, and $D2_A$ motifs (Fig. 5(c)). Electrostatic contributions dominate the stabilization of the water-involved dimers, accounting for 88% ($D1_{AB}$), 72% ($D2_{AB}$), 73% ($D3_{AB}$), and 58% ($D4_{AB}$).

For the molecular pair involving molecule **1** and the second lattice water molecule (O3), two dimers ($D1_{AB}$ and $D2_{AB}$) are identified. $D1_{AB}$ is stabilized by a directional N–H···O hydrogen bond, while $D2_{AB}$ features a directional O–H···N hydrogen bond. Electrostatic energy dominates their stabilization, contributing 79–84%. The second lattice water molecule bridges adjacent molecules of **1** to form an $R_4^4(18)$ motif. In addition, the second lattice water participates in an O–H···O hydrogen bond with the first lattice water molecule, with electrostatic energy accounting for 90% of the stabilization of this water–water dimer ($D1_{AB}$).

3.5. Supramolecular features of compound 2.3H_2O

In the solid-state, the packing arrangement features parallel, extended molecules organized in stacked rows, characteristic of slipped-stacking or columnar packing. The lattice water molecules also align along the crystallographic *a* axis (Fig. 6(a)). To examine the supramolecular features and the energetics of the molecular dimers, CLP-PIXEL energy calculations were performed as described in the experimental section. Pairwise energy analysis shows that three molecular dimers are formed between symmetry-related molecules of (*E*)-*N*′-(1-(pyridine-4-yl)ethylidene)nicotinohydrazide (Table 3 and dimers $D1_A$-$D3_A$), along with one additional dimer ($D1_{AB}$) formed between the same molecule and the first lattice water molecule (O2).

Dimers $D1_A$ and $D2_A$ are stabilized by slipped molecular π-stacking, with interplanar separations of 3.681(6) and 3.741(6) Å and the corresponding slippage distances of 1.269 and 1.803 Å, respectively. These dimers alternate along the structure to form a molecular chain running

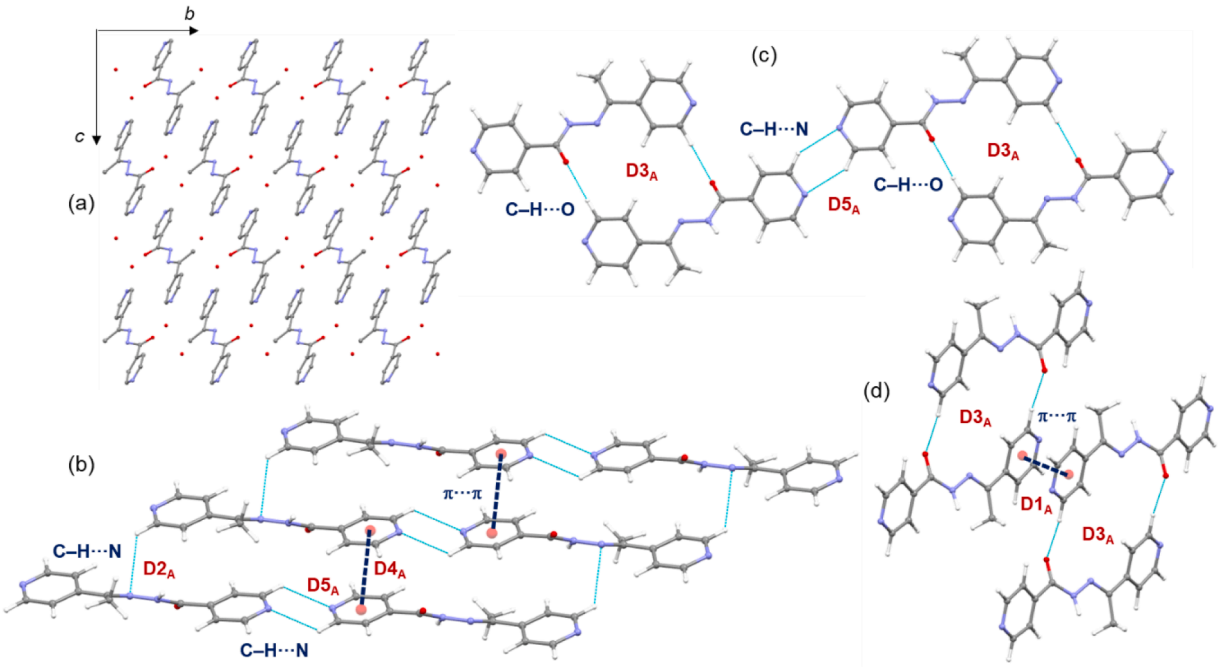

Fig. 4. (a) Crystal packing of **1.2H_2O** viewed along the crystallographic *bc* plane and H atoms have been omitted for clarity, (b) layers of molecule **1** linked by C–H···N and π-stacking interactions, (c) adjacent $D3_A$ dimers connected via the $D5_A$ motif, and (d) adjacent $D3_A$ dimers interconnected via the $D1_A$ motif.

Table 2
Intermolecular interaction energies (E_{tot}) of various molecular dimers of dihydrated compound **1**, calculated using the CLP-PIXEL and DFT methods. All energies are given in kcal mol^{-1}. *Cg*1: N1-C1-C5 and *Cg*2: N4-C9-C13.

Dimer	CD	Symmetry	Important interactions	Geometry[a] H···A (Å), ∠D–H···A (°)	PIXEL MP2/6-31G**					B97D3/ def2TZVP
					E_{Coul}	E_{pol}	E_{disp}	E_{rep}	E_{tot}	ΔE_{cp}
Compound 1. water 1 pair										
$D1_A$	9.170	–*x*+2, –*y*, –*z*+1	*Cg*2···*Cg*2	3.657(7)	–3.2	–0.8	–7.1	4.0	–7.2	–9.8
$D2_A$	6.880	*x*–1, *y*, *z*	C11–H11···N3	2.85, 123	–1.3	–1.3	–9.4	5.4	–6.6	–8.6
$D3_A$	7.490	–*x*+1, –*y*+1, –*z*+1	C12–H12···O1	2.27, 169	–5.4	–1.7	–3.9	5.1	–6.0	–5.9
$D4_A$	9.228	–*x*, –*y*+1, –*z*+2	*Cg*1···*Cg*1	3.689(7)	–1.0	–0.7	–6.1	3.7	–4.1	–6.7
$D5_A$	14.059	–*x*–1, –*y*+1, –*z*+2	C5–H5···N1	2.69, 133	–2.3	–0.8	–2.7	2.5	–3.4	–2.9
$D1_{AB}$	8.419	*x*, *y*, *z*	O2–H2C···N4	1.83, 171	–13.8	–7.2	–2.9	16.6	–7.4	–6.9
$D2_{AB}$	3.381	–*x*+2, –*y*+1, –*z*+1	O2–H2B···N3	2.27, 147	–6.3	–2.6	–3.5	5.9	–6.6	–4.9
			O2–H2B···O1	2.22, 127						
$D3_{AB}$	4.337	–*x*+2, –*y*, –*z*+1	C8–H8C···O2	2.66, 158	–2.2	–0.5	–1.0	0.6	–3.1	–2.9
$D4_{AB}$	6.466	–*x*+1, –*y*+1, –*z*+1	C4–H4···O2	2.69, 150	–1.1	–0.3	–1.0	0.6	–1.8	–1.5
Compound 1. water 2 pair										
$D1_{AB}$	3.393	–*x*, –*y*, –*z*+2	N2–H2···O3	1.87, 166	–11.3	–4.8	–4.2	12.4	–8.0	–4.2
$D2_{AB}$	8.258	*x*, *y*, *z*	O3–H3A···N1	1.98, 165	–10.2	–4.3	–2.7	9.9	–7.3	–6.5
water 1. water 2 pair										
$D1_{AB}$	2.720	*x*+2, *y*, *z*–1	O3–H3B···O2	1.73, 165	–12.1	–5.6	–2.0	15.1	–4.6	–2.4

[a] Neutron values are provided for all D–H···A interactions.

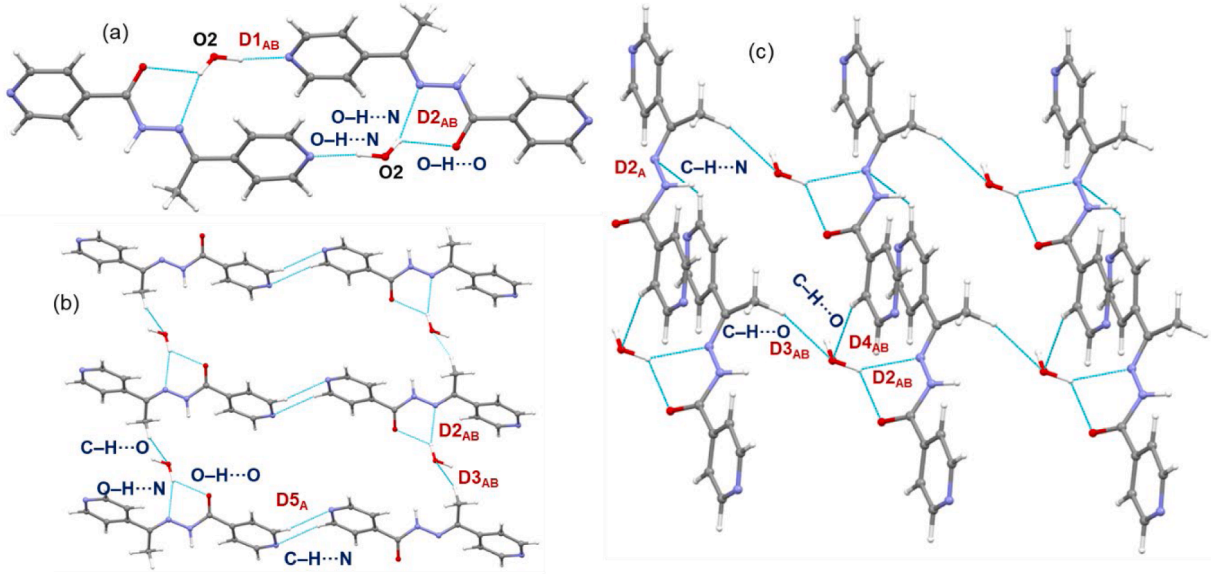

Fig. 5. (a) The first lattice water molecule bridging adjacent molecules of **1** via O–H···N and O–H···O interactions, (b) supramolecular assembly constructed from $D2_{AB}$, $D3_{AB}$, and $D5_A$ motifs, and (c) supramolecular architecture formed by cooperative involvement of $D2_{AB}$, $D3_{AB}$, and $D2_A$ motifs.

parallel to the crystallographic *a* axis. The NCI plot displays green surface regions between the molecules, consistent with weak yet attractive π-stacking interactions (Fig. 6(b)). Differences between intermolecular interaction energies obtained from CLP-PIXEL and DFT calculations arise primarily from dispersion effects. Indeed, the dispersion energy component contributes 63% to the stabilization of dimer $D1_A$ and 71% to that of dimer $D2_A$.

The next weaker dimer, $D3_A$, is stabilized through C–H···N interactions involving the 3-pyridyl groups of neighbouring molecules. This interaction links the molecules across adjacent columns, generating a *C*(4) chain motif. Dispersion energy dominates the stabilization of $D3_A$ as well, contributing 69% of the total stabilization interaction energy. The first lattice water molecule (O2) engages in three interactions, including a bifurcated O–H···O and O–H···N hydrogen bond involving the amide oxygen and hydrazide nitrogen atoms. In addition, the 4-pyridyl ring forms a C–H···O interaction with the water oxygen. These water-mediated contacts support the molecular sheet constructed through C–H···N interactions, as illustrated in Fig. 6(c). CLP-PIXEL calculations show that the stabilization of the $D1_{AB}$ dimer is overwhelmingly electrostatic in nature, with electrostatic contributions accounting for 84% of the total stabilization interaction energy.

In a similar manner, other molecular pair combinations were examined. Molecule **2** and the second lattice water molecule (O3) form two dimers ($D1_{AB}$ and $D2_{AB}$) as depicted in Fig. 7(a). $D1_{AB}$ is stabilized by N–H···O and C–H···O interactions involving the amide N–H and the 3-pyridyl group with the water molecule, whereas $D2_{AB}$ is stabilized by an O–H···N hydrogen bond. Both dimers are predominantly governed by electrostatic contributions, accounting for 75% and 86% of their stabilizing energies, respectively. Notably, these water-mediated motifs interconnect neighbouring molecules of **2**, producing a supramolecular chain extending parallel to the crystallographic *c* axis (Fig. 7(b)).

In contrast, the third lattice water molecule (O4) forms three dimers ($D1_{AB}$-$D3_{AB}$) with molecule **2**, stabilized through O–H···N and C–H···O interactions. The $D1_{AB}$ dimer is dominated by electrostatic stabilization due to its O–H···N hydrogen bond, while the $D2_{AB}$ and $D3_{AB}$ dimers are mainly stabilized by C–H···O interactions, with electrostatic

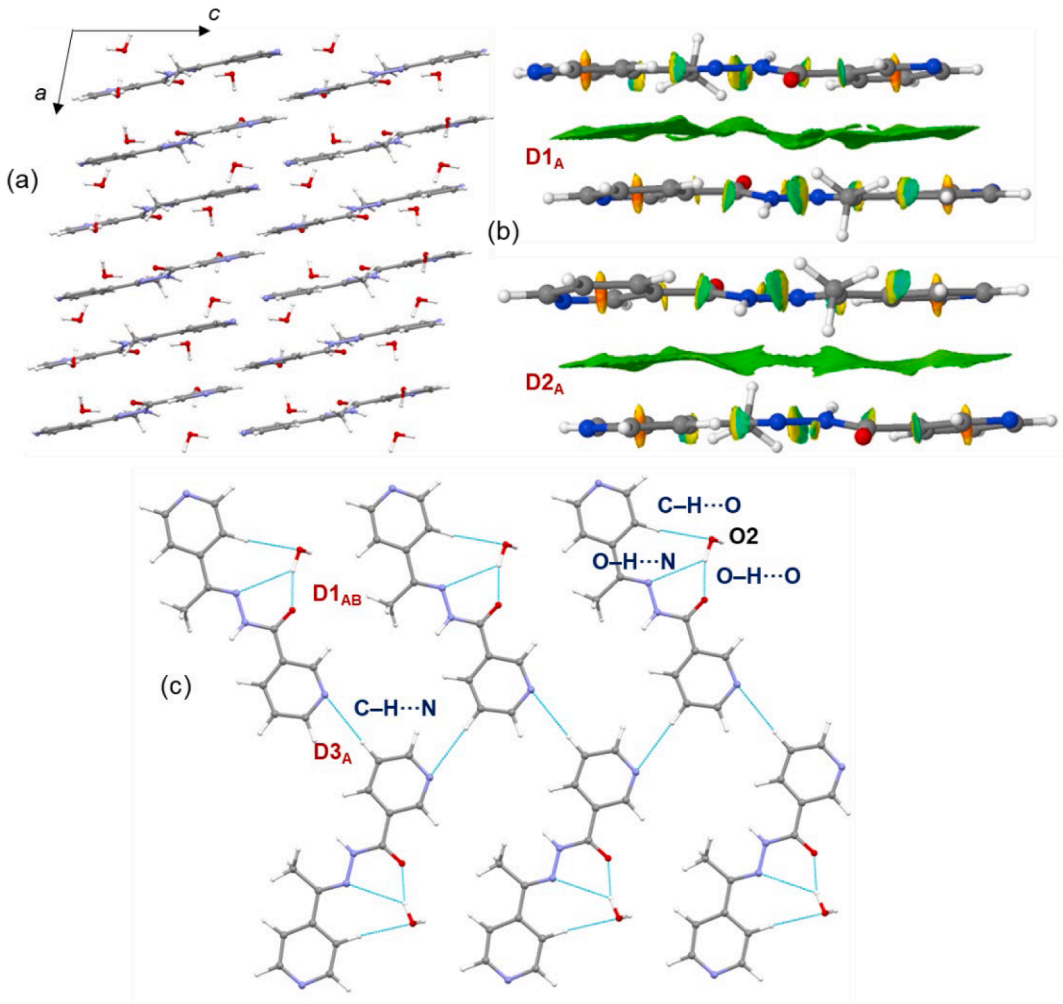

Fig. 6. (a) Columnar crystal packing of trihydrated molecule of **2**, showing the lattice water molecules aligned along the crystallographic *a* axis, (b) green NCI patches between molecules of **2**, indicating attractive weak π-stacking interactions in a slipped arrangement, and (c) a molecular sheet formed through C–H···N interactions involving the 3-pyridyl groups, further supported by water-mediated O–H···N/O and C–H···O interactions.

contributions of 56% and 38%, respectively. As shown in Fig. 7(c), layers of molecule **2** linked via third lattice water molecule form an extended molecular sheet. This water molecule not only connects molecules within the same layer but also bridges molecules between adjacent layers.

Furthermore, each lattice water molecule interacts with the other two through highly directional O–H···O hydrogen bonds (Fig. 7(d)). The NCI plot analysis indicates that a blue surface is observed between the water molecules, confirming the presence of strong O–H···O hydrogen bonds. The strengths of these dimers are comparable across all three cases using both DFT and CLP-PIXEL calculations. As expected, electrostatic energy dominates in all three instances, contributing approximately 90% to their stabilization.

3.6. Topological analysis of hydrogen bonds

The topological properties of the hydrogen bonds present in the hydrated forms of **1** and **2** were analyzed at their bond critical points using Bader's QTAIM approach [50], and the results are summarized in Table 4. Molecular graphs of the selected molecular dimers of **1.2H$_2$O** and **2.3H$_2$O** complexes are shown in Figs. S10 and S11. Positive values of the electron density, ρ(**r**), together with a positive Laplacian ($\nabla^2\rho(\mathbf{r}) > 0$), a positive total electronic energy density (H(**r**) > 0), and the condition -V(**r**)/G(**r**) < 1 indicate closed-shell interactions [51]. In contrast, negative values of the electronic energy density (H(**r**) < 0) combined with -V(**r**)/G(**r**) > 1 suggest interactions of intermediate character, lying between closed-shell and shared-shell interactions. The strengths of the hydrogen bonds were further evaluated using bond dissociation energies calculated according to the approach proposed by Espinosa et al. [52].

In the **1.2H$_2$O** complex, several types of hydrogen bonds are observed, including O–H···N, O–H···O, N–H···O C–H···N, and C–H···O interactions. Of the eleven hydrogen bonds identified, two exhibit an intermediate character between closed- and shared-shell interactions. One of these is an O–H···N hydrogen bond formed between the first lattice water molecule and one of the pyridyl N atoms, with a dissociation energy of 10.2 kcal mol^{-1}. A similar partial covalent nature of water-pyridine O–H···N hydrogen bonds has been reported recently [53], and several other types of hydrogen bonds with partial covalent character have also been described [54]. The second interaction of this type is an O–H···O hydrogen bond between lattice water molecules, which is slightly stronger, with a dissociation energy of 12.4 kcal mol^{-1}. The contour map of the total electronic energy density shows a continuous interaction region between the donor and acceptor atoms, confirming their partial covalent bonding nature (Fig. 8(a,b)).

The remaining nine hydrogen bonds in this complex are classified as closed-shell interactions. The N–H···O hydrogen bond involving the amide NH and a water molecule has a dissociation energy of 7.5 kcal mol^{-1}. The O–H···N interaction between a water molecule and one of the pyridyl N atoms has a strength of 6.1 kcal mol^{-1}, while the corresponding interaction with the hydrazide N atom is weaker, at 2.6 kcal

Table 3
Intermolecular interaction energies (E_{tot}) of various molecular dimers of trihydrated compound **2**, calculated using the CLP-PIXEL and DFT methods. All energies are given in kcal mol^{-1}.

Dimer	CD	Symmetry	Important interactions	Geometry[a] H···A (Å), ∠D–H···A (°)	PIXEL MP2/6-31G**					B97D3/ def2TZVP
					E_{Coul}	E_{pol}	E_{disp}	E_{rep}	E_{tot}	ΔE_{cp}
Compound 2. water 1 pair										
$D1_A$	3.693	–*x*+1, –*y*+1, –*z*+1	Molecular stacking	3.681 (6)	–7.4	–2.1	–16.3	11.1	–14.7	–21.4
$D2_A$	3.789	–*x*+2, –*y*+1, –*z*+1	Molecular stacking	3.741 (6)	–4.3	–1.7	–15.0	10.1	–11.0	–17.0
$D3_A$	12.641	–*x*+1, *y*–1/2, –*z*+3/2	C2–H2A···N1	2.83, 164	–0.4	–0.5	–2.0	1.3	–1.6	–1.5
$D1_{AB}$	3.698	*x*, *y*, *z*	O2–H2B···O1	1.80, 160	–12.9	–4.9	–3.5	12.7	–8.6	–7.1
			O2–H2B···N3	2.80, 132						
			C13–H13···O2	2.51, 167						
Compound 2. water 2 pair										
$D1_{AB}$	3.656	–*x*+2, –*y*+1, –*z*+1	N2–H2···O3	2.12, 163	–8.4	–2.8	–3.7	6.5	–8.5	–5.6
			C3–H3···O3	2.51, 118						
$D2_{AB}$	8.255	–*x*+2, *y*+1/2, –*z*+1/2	O3–H3A···N4	1.89, 161	–12.3	–6.0	–2.9	14.1	–7.1	–6.4
Compound 2. water 3 pair										
$D1_{AB}$	7.245	–*x*+2, –*y*, –*z*+1	O4–H4A···N1	1.82, 170	–13.2	–6.9	–3.4	17.5	–5.9	–5.4
$D2_{AB}$	8.352	*x*–1, –*y*+1/2, *z*+1/2	C1–H1···O4	2.61, 126	–1.3	–0.7	–1.6	1.6	–2.0	–0.9
$D3_{AB}$	4.627	−*x*+2, −*y*+1, −*z*+1	C3–H3···O4	2.67, 163	–0.4	–0.8	–2.0	1.5	–1.7	–1.0
water 1. water 2 pair										
$D1_{AB}$	2.730	*x*, *y*, *z*	O3–H3B···O2	1.73, 167	–12.8	–5.7	–2.0	14.6	–5.8	–3.1
water 1. water 3 pair										
$D1_{AB}$	2.764	*x*–1, *y*, *z*	O2–H2C···O4	1.76, 174	–12.1	–5.0	–1.8	13.2	–5.8	–3.4
water 2. water 3 pair										
$D1_{AB}$	2.806	*x*, *y*, *z*	O4–H4B···O3	1.83, 165	–9.7	–4.2	–1.8	10.2	–5.4	–3.3

[a] Neutron values are provided for all D–H···A interactions.

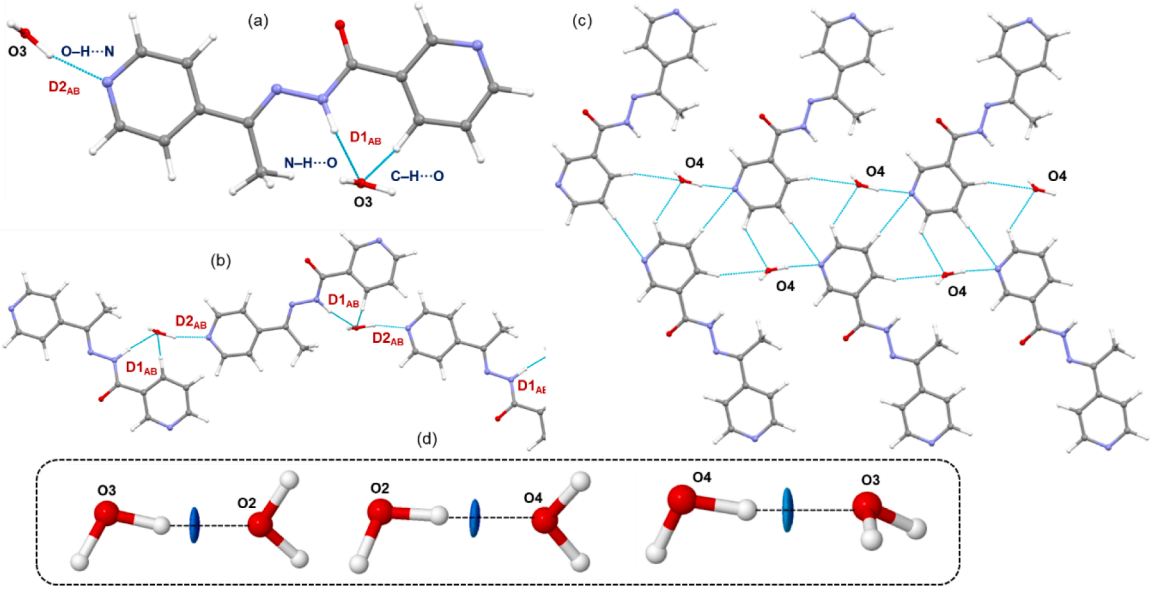

Fig. 7. (a) Interaction between molecule **2** and lattice water molecule 2, (b) a water-mediated supramolecular chain formed through N–H···O, O–H···N, and C–H···O interactions, (c) a supramolecular sheet built from C–H···N interactions together with water mediated O–H···N and C–H···O interactions involving lattice water molecule 3, and (d) cooperative interactions among lattice water molecules through directional O–H···O hydrogen bonds, with a blue surface between water molecules, indicating strong attractive noncovalent interactions.

mol^{-1}. The O–H···O hydrogen bond between a water molecule and amide carbonyl oxygen has a dissociation energy of 2.8 kcal mol^{-1}. The weaker C–H···O interaction has a dissociation energy of 1.0 kcal mol^{-1}, and the C–H···N interactions fall in the range of 0.8 to 1.2 kcal mol^{-1}.

Similar to the **1.2H$_2$O** complex, the **2.3H$_2$O** complex also exhibits a variety of hydrogen bonds, including O–H···N, O–H···O, N–H···O, C–H···N, and C–H···O interactions across different molecular pairs. Notably, this complex shows a larger number of hydrogen bonds with intermediate bonding character between closed- and shared-shell interactions, as indicated by the QTAIM topological parameters, compared with the **1.2H$_2$O** complex. Specifically, five out of twelve hydrogen bonds display this intermediate bonding nature (Fig. 8(c-h)). Among these, two O–H···O hydrogen bonds formed between lattice water molecules exhibit dissociation energies of 11.1 and 12.2 kcal mol^{-1}, closely matching both the strength and bonding character observed in the **1.2H$_2$O** complex. Another O–H···O hydrogen bond occurs between a water molecule and a carbonyl oxygen atom, with a dissociation energy of 9.9 kcal mol^{-1}. The remaining two intermediate interactions are O–H···N hydrogen bonds, with dissociation energies of 10.4 and 8.4 kcal mol^{-1}, formed between water molecules and the 3-pyridyl/4-pyridyl N atoms, respectively. Although similar O–H···N interactions are also present in the **1.2H$_2$O** complex, their bonding character and strengths differ between the two hydrated forms. It is of interest to note that, as observed in the **1.2H$_2$O** complex, the water-pyridine dimer formed

Table 4
Topological parameters for selected intermolecular interactions in different dimers of **1.2H_2O** and **2.3H_2O**. R_{ij}, Bond path (Å); $\rho(\mathbf{r})$, Electron density (e Å^{-3}); $\nabla^2\rho(\mathbf{r})$, Laplacian of electron density (e Å^{-5}); $V(\mathbf{r})$, Potential electron density (kJ mol^{-1} br^{-3}); $G(\mathbf{r})$, Kinetic electron density (kJ mol^{-1} br^{-3}); $H(\mathbf{r})$, Total electronic energy density (kJ mol^{-1} br^{-3}); D_e, Dissociation energy (kcal mol^{-1}).

Dimer	Interaction	R_{ij}	$\rho(\mathbf{r})$	$\nabla^2\rho(\mathbf{r})$	$V(\mathbf{r})$	$G(\mathbf{r})$	$H(\mathbf{r})$	$\lvert\frac{-V(r)}{G(r)}\rvert$	D_e
Compound 1.2H_2O									
Compound 1/water 1 pair									
$D2_A$	C11–H11···N3	2.893	0.035	0.424	−7.0	9.3	2.3	0.76	0.8
$D3_A$	C12–H12···O1	2.287	0.077	1.140	−18.4	24.7	6.3	0.74	2.2
$D5_A$	C5–H5···N1	2.724	0.046	0.558	−9.6	12.4	2.8	0.78	1.2
$D1_{AB}$	O2–H2C···N4	1.854	0.254	2.352	−84.7	74.4	−10.3	1.14	10.2
$D2_{AB}$	O2–H2B···N3	2.299	0.092	1.178	−21.3	26.7	5.4	0.80	2.6
	O2–H2B···O1	2.256	0.089	1.429	−23.3	31.1	7.8	0.75	2.8
$D3_{AB}$	C8–H8C···O2	2.683	0.038	0.494	−8.1	10.8	2.7	0.75	1.0
$D4_{AB}$	C4–H4···O2	2.709	0.041	0.486	−8.1	10.7	2.6	0.76	1.0
Compound 1/water 2 pair									
$D1_{AB}$	N2–H2···O3	1.898	0.182	2.750	−62.2	68.6	6.4	0.91	7.5
$D2_{AB}$	O3–H3A···N1	2.003	0.177	1.965	−51.0	52.3	1.2	0.98	6.1
water 1/water 2 pair									
$D1_{AB}$	O3–H3B···O2	1.757	0.257	3.313	−103.3	96.8	−6.5	1.07	12.4
Compound 2.3H_2O									
Compound 2/water 1 pair									
$D3_A$	C2–H2A···N1	2.853	0.032	0.404	−6.8	8.9	2.1	0.76	0.80
$D1_{AB}$	O2–H2B···O1	1.823	0.218	2.991	−82.3	81.9	−0.4	1.00	9.9
	C13–H13···O2	2.537	0.052	0.671	−10.9	14.6	3.7	0.75	1.3
Compound 2/water 2 pair									
$D1_{AB}$	N2–H2···O3	2.148	0.109	1.606	−28.3	36.0	7.7	0.79	3.4
	C3–H3···O3	2.598	0.065	0.892	−16.1	20.2	4.1	0.80	1.9
$D2_{AB}$	O3–H3A···N4	1.913	0.222	2.262	−70.0	65.8	−4.2	1.06	8.4
Compound 2/water 3 pair									
$D1_{AB}$	O4–H4A···N1	1.847	0.256	2.457	−86.8	76.9	−9.9	1.13	10.4
$D2_{AB}$	C1–H1···O4	2.649	0.052	0.672	−11.6	15.0	3.3	0.78	1.4
$D3_{AB}$	C3–H3···O4	2.693	0.034	0.504	−7.7	10.7	3.0	0.72	0.9
water 1/water 2 pair									
$D1_{AB}$	O3–H3B···O2	1.753	0.253	3.350	−101.7	96.5	-5.2	1.05	12.2
water 1/water 3 pair									
$D1_{AB}$	O2–H2C···O4	1.781	0.237	3.159	−92.7	89.4	-3.3	1.04	11.1
water 2/water 3 pair									
$D1_{AB}$	O4–H4B···O3	1.855	0.203	2.781	−74.2	75.0	0.8	0.99	8.9

through O–H···N hydrogen bonds exhibits an uninterrupted region between the interacting atoms (Fig. 8(d,e)), confirming their partial covalent character. In contrast, the other four dimers (Fig. 8(c,f-h) show an interrupted region due to higher values (less negative values) of the total electronic energy density $H(r)$ compared with hydrogen bonds of partial covalent nature.

In addition, an O–H···O hydrogen bond between water molecules is classified as a closed-shell interaction, with a dissociation energy of 8.9 kcal mol^{-1}. The N–H···O hydrogen bond involving the amide NH group and a water molecule is also of closed-shell type but is comparatively weaker, with a dissociation energy of 3.4 kcal mol^{-1}, lower than that observed in the **1.2H_2O** complex. The partial covalent character of N–H···O hydrogen bonds in pyrimidine-5-carbonitriles [55] and N–H···N hydrogen bonds in *N*-substituted-5-(adamantan-1-yl)-1,3,4-thiadiazole-2-amines [56] was assessed using the QTAIM framework. The C–H···O interactions exhibit dissociation energies in the range of 0.9-1.9 kcal mol^{-1}, while the C–H···N interaction is weaker, at 0.8 kcal mol^{-1}. Overall, this QTAIM analysis provides detailed insight into the nature and relative strengths of the hydrogen bonding interactions and highlights their cooperative role in stabilizing the hydrated isomeric structures.

3.7. Experimental and theoretical UV-Vis absorption

The UV–Vis absorption spectra of compounds **1** and **2** ($c = 5 \times 10^{-5}$ M) were recorded in DMSO at room temperature. Both compounds exhibit intense absorption band at 289 nm for **1** and 293 nm for **2**, which can be attributed to n–π* transitions associated with the >C=N–N chromophore [46]. These experimental features are well reproduced by time-dependent DFT (TD-DFT) calculations performed in DMSO (Fig. S12). The calculated absorption maxima at 309 nm for compound **1** (oscillator strength (f) = 0.6704) and 303 nm for compound **2** (oscillator strength (f) = 0.7835), both dominated by HOMO→LUMO transitions (97% and 95%, respectively). Overall, the calculated λ_{max} values show good agreement with the experimental data (Table 5).

Frontier molecular orbital analysis reveals HOMO and LUMO energies of −6.949 eV and −2.424 eV for compound **1**, and −6.909 eV and −2.319 eV for compound **2**, resulting in comparable energy gaps of 4.5 eV and 4.6 eV, respectively. These results indicate that isomeric effects have only a minor influence on the electronic structure. Consistently, both compounds display similar electron density distributions in their frontier orbitals (Fig. S13), with the LUMO electron density covers the entire molecular framework, while the HOMO shows the reduced localization on the pyridine ring adjacent to the C=O group. Comparable observations have been reported in the literature when examining isomeric effects [57,58].

The calculated global reactivity descriptors further support the close electronic resemblance between the two compounds, while highlighting subtle differences in their reactivity profiles (Table 6). Compound **2** exhibits a slightly larger energy gap and higher chemical hardness, suggesting greater stability and lower polarizability. In contrast, compound **1** shows a higher electrophilicity index, indicating a stronger tendency to accept electrons and interact with nucleophilic sites. This enhanced electrophilic character may contribute to stronger intermolecular interactions and could be relevant for understanding differences in their biological behaviour. Overall, while both compounds are electronically stable and moderately reactive, compound **1** exhibits slightly higher electrophilicity and softness, favouring stronger intermolecular

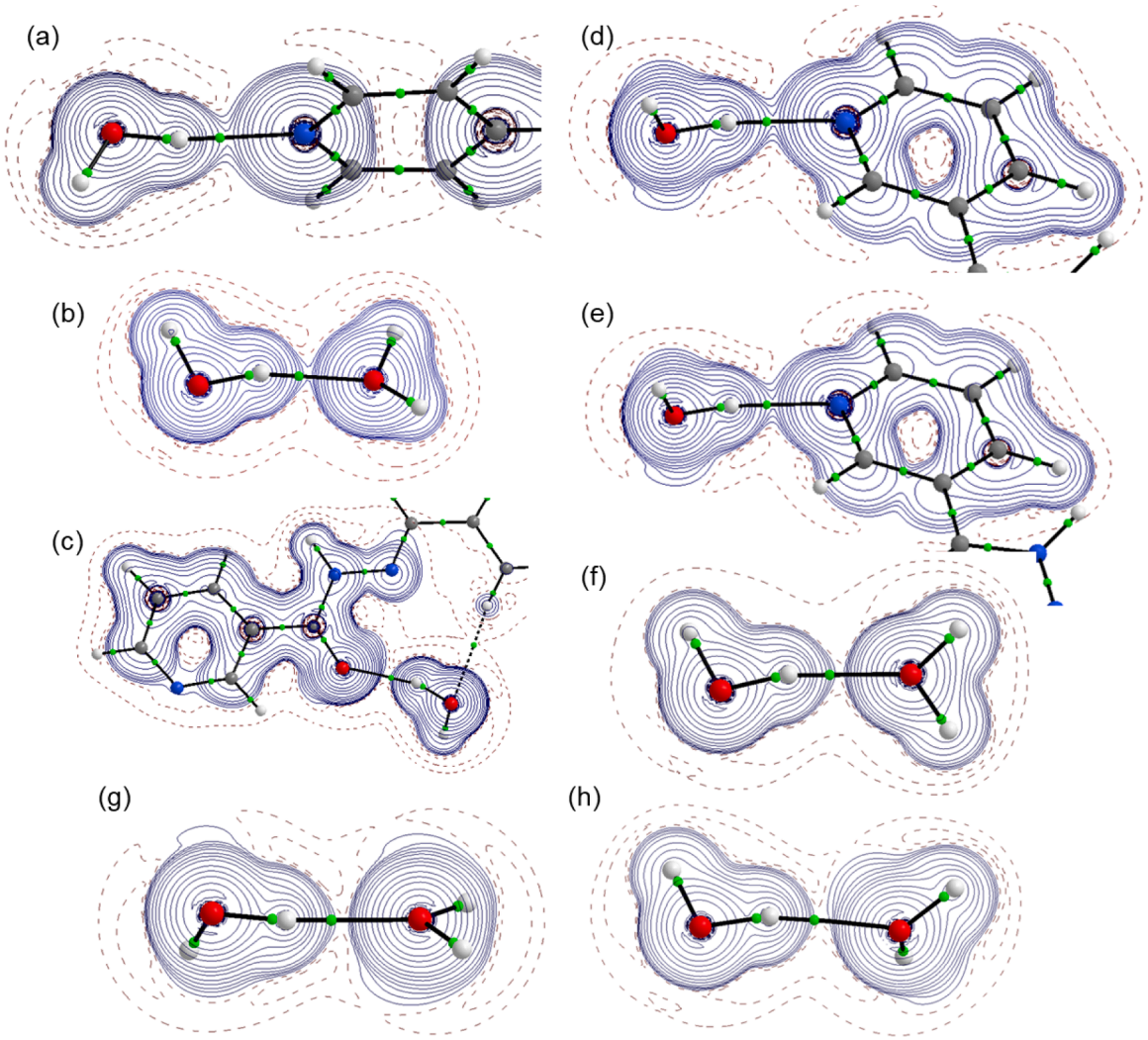

Fig. 8. Total electronic energy density distribution, $H(\mathbf{r})$, illustrating strong intermolecular O–H···N and O–H···O hydrogen bonds in the (a,b) **1.2H$_2$O** and (c-h) **2.3H$_2$O** complexes: (a) $D1_{AB}$ (O2–H2C···N4), (b) $D1_{AB}$ (O3–H3B···O2), (c) $D1_{AB}$ (O2–H2B···O1), (d) $D2_{AB}$ (O3–H3A···N4), (e) $D1_{AB}$ (O4–H4A···N1), (f) $D1_{AB}$ (O3–H3B···O2), (g) $D1_{AB}$ (O2–H2C···O4), and (h) $D1_{AB}$ (O4–H4B···O3). All plots are drawn in the plane of the interacting atoms; green spheres denote bond critical points.

Table 5
Excitation wavelengths (in nm), configuration and oscillator strengths for the compounds **1** and **2**.

Compound	Main configuration (%)	TD-DFT (in DMSO) at B3LYP/6-311++G(d,p)				Experimental (λ_{max})
		λ_{max}	f	HOMO (eV)	LUMO (eV)	Solvent (in DMSO)
1	H → L (97%)	309	0.6704	−6.949	−2.424	289
2	H → L (95%)	303	0.7835	−6.909	−2.319	293

Table 6
The calculated quantum chemical descriptors of compounds **1** and **2**.

Parameter	Formula	Compound **1** (eV)	Compound **2** (eV)
Ionization potential (I)	$-E_{HOMO}$	6.949	6.909
Electron affinity (A)	$-E_{LUMO}$	2.424	2.319
Energy gap (ΔE)	$E_{LUMO} - E_{HOMO}$	4.525	4.590
Chemical hardness (η)	(I − A)/2	2.263	2.295
Chemical softness (S)	1/(2η)	0.221	0.218
Chemical potential (μ)	−(I + A)/2	−4.687	−4.614
Electronegativity (χ)	(I + A)/2	4.687	4.614
Electrophilicity index (ω)	$\mu^2/(2\eta)$	4.85	4.64

interactions, whereas compound **2** is marginally more stable and less reactive, which may influence its binding affinity and biological performance.

3.8. Thermogravimetric analysis (TGA)

The thermal behaviour of the lattice water molecules in compounds **1** and **2** was examined using TGA (Figs. S14 and S15). In compound **1**, the first weight-loss step observed between 20 and 134°C is attributed to the release of lattice water, followed by a second major mass loss above 237°C, corresponding to decomposition of the organic framework. Considering the presence of two lattice water molecules and an

anhydrous molecular weight of 240.27 g mol^{-1}, the theoretical dehydration loss is calculated to be 13.04% using the expression $\frac{n\times 18.015}{M+(n\times 18.015)} \times 100$, where n is the number of lattice water molecules, M is the molecular weight of the anhydrous compound, and 18.015 g mol^{-1} is the molecular weight of a water molecule. This calculated value is in good agreement with the experimentally observed mass loss, confirming the lattice water content inferred from the crystal structure.

In contrast, compound **2** exhibits lattice water loss over a much narrower temperature range of 61–97°C, followed by a second decomposition step above 244°C. For this compound, which contains three lattice water molecules and has the same anhydrous molecular weight of 240.27 g mol^{-1}, the theoretical dehydration loss is calculated to be 18.36%. The close correspondence between the experimental and calculated mass losses further validates the crystallographic assignment of lattice water.

The distinct dehydration behaviours of the two compounds can be rationalized on the basis of their solid-state structures. The broad dehydration range observed for compound **1** suggests that its lattice water molecules occupy crystallographically non-equivalent environments and engage in hydrogen bonds of varying strengths, leading to a gradual release upon heating. In contrast, the narrow dehydration range for compound **2** indicates that the lattice water molecules experience more uniform hydrogen-bonding environments and undergo a more cooperative dehydration process.

4. Conclusions

We have elucidated the structural and interaction landscapes of two isomeric hydrated nicotinoyl-hydrazones, **1·2H₂O** and **2·3H₂O**, through combined crystallographic, spectroscopic, and computational analysis. Although both compounds share similar molecular geometries, their hydration patterns and hydrogen-bonding architectures differ substantially, reflecting the influence of pyridyl substitution on supramolecular assembly. Hirshfeld surface and fingerprint analyses demonstrate that the dominant intermolecular contacts are mediated by hydrogen bonds involving lattice water molecules, with quantitative differences linked to the additional water in **2·3H₂O**. Energy decomposition reveals that strong hydrogen bonds are driven by electrostatic stabilization, while dispersion interactions contribute significantly to π–π and C–H based contacts. QTAIM topological parameters indicate that certain O–H···N and O–H···O interactions possess intermediate bonding character, consistent with partial covalent behaviour. These findings deepen our understanding of how hydrogen-bonding networks shape solid-state stability in hydrated organic systems. Complementary UV–Vis absorption and TD-DFT studies show that electronic properties are only marginally affected by isomerism, underscoring the dominant role of intermolecular interactions in determining material behaviour. This work advances the fundamental framework for interpreting hydration effects, hydrogen-bonding cooperativity, and structure–property relationships in molecular liquids and related condensed phases, with potential implications for design strategies in soft materials, liquid crystals, and hydrogen-bonded liquids.

Data availability

CCDC 2518006, 2517873 contain the supplementary crystallographic data for this paper. These data correspond to **1.2H₂O** and **2.3H₂O** and can be obtained freely via http://www.ccdc.cam.ac.uk/data_request/cif or by emailing to data_request@ccdc.cam.ac.uk or by contacting directly the Cambridge Crystallographic Data Centre, 12 Union Road, Cambridge CB2 1EZ, UK; fax: +44 1223 336 033.

CRediT authorship contribution statement

Suman Adhikari: Writing – original draft, Methodology, Investigation, Formal analysis, Conceptualization. **Ravichandran Deepa Roshini:** Writing – original draft, Visualization, Methodology, Investigation, Formal analysis. **Ghodrat Mahmoudi:** Project administration, Funding acquisition, Conceptualization. **Asmet N. Azizova:** Resources. **Olivier Blacque:** Validation, Software, Resources, Data curation. **M. Judith Percino:** Software, Resources, Data curation. **Subbiah Thamotharan:** Writing – original draft, Visualization, Validation, Software, Investigation, Formal analysis, Data curation, Conceptualization.

Declaration of competing interest

The authors declare that they have no known competing financial interests or personal relationships that could have appeared to influence the work reported in this paper.

Acknowledgements

S.A. acknowledges support from the Govt. Degree College, Dharmanagar, Tripura(N), 799253, India. ST expresses sincere gratitude to the management of SASTRA Deemed University for awarding the SASTRA Indo-Mexico G20 Chair faculty position. S.T. and M.J.P. also thank the Laboratorio Nacional de Supercómputo del Sureste (LNS-BUAP) and SASTRA Deemed University for providing computational resources.

Supplementary materials

Supplementary material associated with this article can be found, in the online version, at doi:10.1016/j.molstruc.2026.145484.

References

[1] I. Alkorta, J. Elguero, A. Frontera, Not only hydrogen bonds: other noncovalent interactions, Crystals 10 (2020) 180, https://doi.org/10.3390/cryst10030180.
[2] J. Chen, Q. Peng, X. Peng, H. Zhang, H. Zeng, Probing and Manipulating noncovalent interactions in functional polymeric systems, Chem. Rev. 122 (2022) 14594–14678, https://doi.org/10.1021/acs.chemrev.2c00215.
[3] S. Jena, J. Dutta, K.D. Tulsiyan, A.K. Sahu, S.S. Choudhury, H.S. Biswal, Noncovalent interactions in proteins and nucleic acids: beyond hydrogen bonding and π-stacking, Chem. Soc. Rev. 51 (2022) 4261–4286, https://doi.org/10.1039/D2CS00133K.
[4] S. Adhikari, A. Datta, I. Saha, K. Ghosh, Synthetic receptors for urea and barbiturates: an overview, Coord. Chem. Rev. 517 (2024) 215989, https://doi.org/10.1016/j.ccr.2024.215989.
[5] T. Bhattacharjee, S. Nath, S. Roy, R.M. Gomila, O. Sahin, W. Kaminsky, A. Frontera, S. Adhikari, Insights into supramolecular networks engineered via tetrel and hydrogen bonding interactions in Hemidirected lead(ii) complexes, Cryst. Growth Des. 25 (2025) 8601–8615, https://doi.org/10.1021/acs.cgd.5c00996.
[6] X. Song, Y. Wang, C. Wang, D. Wang, G. Zhuang, K.O. Kirlikovali, P. Li, O.K. Farha, Design rules of hydrogen-bonded organic frameworks with high chemical and thermal stabilities, J. Am. Chem. Soc. 144 (2022) 10663–10687, https://doi.org/10.1021/jacs.2c02598.
[7] H.A. Fargher, T.J. Sherbow, M.M. Haley, D.W. Johnson, M.D. Pluth, C–H···S hydrogen bonding interactions, Chem. Soc. Rev. 51 (2022) 1454–1469, https://doi.org/10.1039/D1CS00838B.
[8] S. Maity, V.K. Deb, S. Mondal, A. Chakraborty, K. Pramanick, S. Adhikari, Leveraging supramolecular systems in biomedical breakthroughs, Biofactors 51 (2025) e70005, https://doi.org/10.1002/biof.70005.
[9] Y. Liu, L. Wang, L. Zhao, Y. Zhang, Z.-T. Li, F. Huang, Multiple hydrogen bonding driven supramolecular architectures and their biomedical applications, Chem. Soc. Rev. 53 (2024) 1592–1623, https://doi.org/10.1039/D3CS00705G.
[10] J. Bae, S.H. Park, D. Moon, N.C. Jeong, Crystalline hydrogen bonding of water molecules confined in a metal-organic framework, Commun. Chem. 5 (2022) 51, https://doi.org/10.1038/s42004-022-00666-8.
[11] A.J. Rieth, K.M. Hunter, M. Dincă, F. Paesani, Hydrogen bonding structure of confined water templated by a metal-organic framework with open metal sites, Nat. Commun. 10 (2019) 4771, https://doi.org/10.1038/s41467-019-12751-z.
[12] K. Ghosh, S. Adhikari, R. Fröhlich, Water templated hydrogen-bonded network of pyridine amide appended carbamate in solid state, J. Mol. Struct. 785 (2006) 63–67, https://doi.org/10.1016/j.molstruc.2005.09.032.

[13] P. Li, M.R. Ryder, J.F. Stoddart, Hydrogen-bonded organic frameworks: a rising class of porous molecular materials, Accounts Mater. Res. 1 (2020) 77–87, https://doi.org/10.1021/accountsmr.0c00019.

[14] R.-B. Lin, B. Chen, Hydrogen-bonded organic frameworks: chemistry and functions, Chem 8 (2022) 2114–2135, https://doi.org/10.1016/j.chempr.2022.06.015.

[15] S. Rollas, S.G. Küçükgüzel, Biological activities of hydrazone derivatives, Molecules 12 (2007) 1910–1939, https://doi.org/10.3390/12081910.

[16] L.A. Tatum, X. Su, I. Aprahamian, Simple Hydrazone Building Blocks for Complicated Functional Materials, Acc. Chem. Res. 47 (2014) 2141–2149, https://doi.org/10.1021/ar500111f.

[17] X. Su, I. Aprahamian, Hydrazone-based switches, metallo-assemblies and sensors, Chem. Soc. Rev. 43 (2014) 1963–1981, https://doi.org/10.1039/C3CS60385G.

[18] S. Adhikari, S. Nath, S. Kansız, N. Balidya, A.K. Paul, N. Dege, O. Sahin, G. Mahmoudi, A.K. Verma, D.A. Safin, Zinc(II) coordination compound with N′-(pyridin-2-ylmethylene)nicotinohydrazide: synthesis, crystal structure, computational and cytotoxicity studies, J. Inorg. Biochem. 257 (2024) 112598, https://doi.org/10.1016/j.jinorgbio.2024.112598.

[19] S. Adhikari, A. Hussain Sheikh, N. Baildya, G. Mahmoudi, N. Alam Choudhury, O. Okpareke, T. Sen, A. Kumar Verma, R. Kumar Singh, S. Pathak, W. Kaminsky, Antiproliferative evaluation and supramolecular properties of a Pd(II) complex harvested from benzil bis(pyridyl hydrazone) ligand: combined experimental and theoretical studies, Inorg. Chem. Commun. 152 (2023) 110646, https://doi.org/10.1016/j.inoche.2023.110646.

[20] N. T.N, S. Sasi, Therapeutic potential of dihydrazones and their metal complexes: a comprehensive review, Polyhedron 283 (2026) 117830, https://doi.org/10.1016/j.poly.2025.117830.

[21] S. Nath, V.K. Deb, N. Baildya, S. Roy, W. Kaminsky, A. Kumar Verma, S. Hussain, S. Demir Kanmazalp, G. Mahmoudi, A.N. Azizova, S. Adhikari, I. Saha, Synthesis, structural analysis, computational investigation, and cytotoxicity studies of new copper(II) coordination polymers, J. Mol. Struct. 1348 (2025) 143124, https://doi.org/10.1016/j.molstruc.2025.143124.

[22] S. Nath, R.J. Butcher, W. Kaminsky, S. Adhikari, A.N. Azizova, Ö.F. Tutar, E. V Panova, G. Mahmoudi, R.M. Gomila, A. Frontera, D.A. Safin, A structural versatility of the lead(II) coordination compounds with N′-(pyridin-2-ylmethylene) isonicotinohydrazide, Inorg. Chem. Commun. 182 (2025) 115459, https://doi.org/10.1016/j.inoche.2025.115459.

[23] C.F. Macrae, I. Sovago, S.J. Cottrell, P.T.A. Galek, P. McCabe, E. Pidcock, M. Platings, G.P. Shields, J.S. Stevens, M. Towler, P.A. Wood, Mercury 4.0: from visualization to analysis, design and prediction, J. Appl. Crystallogr. 53 (2020) 226–235, https://doi.org/10.1107/S1600576719014092.

[24] R.C. Clark, J.S. Reid, The analytical calculation of absorption in multifaceted crystals, Acta Crystallogr. Sect. A. 51 (1995) 887–897, https://doi.org/10.1107/S0108767395007367.

[25] O.V Dolomanov, L.J. Bourhis, R.J. Gildea, J.A.K. Howard, H. Puschmann, OLEX2: a complete structure solution, refinement and analysis program, J. Appl. Crystallogr. 42 (2009) 339–341, https://doi.org/10.1107/S0021889808042726.

[26] G. Sheldrick, SHELXT - integrated space-group and crystal-structure determination, Acta Crystallogr. Sect. A. 71 (2015) 3–8, https://doi.org/10.1107/S2053273314026370.

[27] G. Sheldrick, Crystal structure refinement with SHELXL, Acta Crystallogr. Sect. C. 71 (2015) 3–8, https://doi.org/10.1107/S2053229614024218.

[28] A. Spek, Structure validation in chemical crystallography, Acta Crystallogr. Sect. D. 65 (2009) 148–155, https://doi.org/10.1107/S090744490804362X.

[29] M.J. Frisch, G.W. Trucks, H.B. Schlegel, G.E. Scuseria, M.A. Robb, J.R. Cheeseman, G. Scalmani, V. Barone, B. Mennucci, G.A. Petersson, H. Nakatsuji, M. Caricato, X. Li, H.P. Hratchian, A.F. Izmaylov, J. Bloino, G. Zheng, J.L. Sonnenberg, M. Hada, M. Ehara, K. Toyota, R. Fukuda, J. Hasegawa, M. Ishida, T. Nakajima, Y. Honda, O. Kitao, H. Nakai, T. Vreven, J.A. Montgomery Jr, J.E. Peralta, F. Ogliaro, M. J. Bearpark, J. Heyd, E.N. Brothers, K.N. Kudin, V.N. Staroverov, R. Kobayashi, J. Normand, K. Raghavachari, A.P. Rendell, J.C. Burant, S.S. Iyengar, J. Tomasi, M. Cossi, N. Rega, N.J. Millam, M. Klene, J.E. Knox, J.B. Cross, V. Bakken, C. Adamo, J. Jaramillo, R. Gomperts, R.E. Stratmann, O. Yazyev, A.J. Austin, R. Cammi, C. Pomelli, J.W. Ochterski, R.L. Martin, K. Morokuma, V.G. Zakrzewski, G.A. Voth, P. Salvador, J.J. Dannenberg, S. Dapprich, D.A. Daniels, O. Farkas, J. B. Foresman, J.V. Ortiz, J. Cioslowski, D.J. Fox, Gaussian 09, Revision D.01, Gaussian Inc, Wallingford, CT, USA, 2013.

[30] F.H. Allen, I.J. Bruno, Bond lengths in organic and metal-organic compounds revisited: X—H bond lengths from neutron diffraction data, Acta Crystallogr. Sect. B. 66 (2010) 380–386, https://doi.org/10.1107/S0108768110012048.

[31] P.R. Spackman, M.J. Turner, J.J. McKinnon, S.K. Wolff, D.J. Grimwood, D. Jayatilaka, M.A. Spackman, CrystalExplorer: a program for Hirshfeld surface analysis, visualization and quantitative analysis of molecular crystals, J. Appl. Crystallogr. 54 (2021) 1006–1011, https://doi.org/10.1107/S1600576721002910.

[32] A. Gavezzotti, Efficient computer modeling of organic materials. The atom–atom, Coulomb–London–Pauli (AA-CLP) model for intermolecular electrostatic-polarization, dispersion and repulsion energies, New J. Chem. 35 (2011) 1360–1368, https://doi.org/10.1039/C0NJ00982B.

[33] A. Gavezzotti, Calculation of intermolecular interaction energies by direct numerical integration over electron densities. 2. An improved polarization model and the evaluation of dispersion and repulsion energies, J. Phys. Chem. B. 107 (2003) 2344–2353, https://doi.org/10.1021/jp022288f.

[34] M. Udayakumar, M. Cerón, P. Ceballos, M.J. Percino, S. Thamotharan, Interplay of weak noncovalent interactions in two conjugated positional isomers: A combined X-ray, optical properties and theoretical investigation, J. Mol. Struct. 1195 (2019) 32–42, https://doi.org/10.1016/j.molstruc.2019.05.109.

[35] L.H. Al-Wahaibi, G. Akilandeswari, R. Anusha, N.H. Al-Shaalan, O.M. Alkmali, A. A. El-Emam, J.M. Percino, S. Thamotharan, Insights into the nature of weak noncovalent interactions in 3-(4-fluorophenyl)-6-(2-fluorophenyl)-1,2,4-triazolo [3,4-b][1,3,4]thiadiazole, a potential bioactive agent: X-ray, QTAIM and molecular docking analysis, J. Mol. Struct. 1183 (2019) 331–341, https://doi.org/10.1016/j.molstruc.2019.01.106.

[36] Y.V. Govindaraj Sangeetha, B. Manikandan, S. Selva Ganesan, O. Blacque, M. J. Percino, S. Thamotharan, Investigation of the role of fluorine position in benzoxanthene derivatives in supramolecular assembly: an experimental and theoretical exploration, J. Indian Chem. Soc. 102 (2025) 102266, https://doi.org/10.1016/j.jics.2025.102266.

[37] L.H. Al-Wahaibi, A. Chakraborty, E.T. Warda, O. Blacque, H.M. Hassan, M. J. Percino, A.A. El-Emam, S. Thamotharan, Experimental and computational investigations of two N′-(adamantan-2-ylidene)-substituted benzohydrazide derivatives: crystal structures, antiproliferative activity, molecular docking, and molecular dynamics simulations, Struct. Chem. 36 (2025) 2319–2336, https://doi.org/10.1007/s11224-025-02512-8.

[38] F. Weigend, Accurate Coulomb-fitting basis sets for H to Rn, Phys. Chem. Chem. Phys. 8 (2006) 1057–1065, https://doi.org/10.1039/B515623H.

[39] S. Grimme, S. Ehrlich, L. Goerigk, Effect of the damping function in dispersion corrected density functional theory, J. Comput. Chem. 32 (2011) 1456–1465, https://doi.org/10.1002/jcc.21759.

[40] S.F. Boys, F. Bernardi, The calculation of small molecular interactions by the differences of separate total energies. Some procedures with reduced errors, Mol. Phys. 19 (1970) 553–566, https://doi.org/10.1080/00268977000101561.

[41] T.A. Keith, AIMAll, ver. 19.02.13, TK Gristmill Software, Overland Park, KS, 2019.

[42] Y. Zhao, D.G. Truhlar, The M06 suite of density functionals for main group thermochemistry, thermochemical kinetics, noncovalent interactions, excited states, and transition elements: two new functionals and systematic testing of four M06-class functionals and 12 other function, Theor. Chem. Acc. 120 (2008) 215–241, https://doi.org/10.1007/s00214-007-0310-x.

[43] J. Contreras-García, E.R. Johnson, S. Keinan, R. Chaudret, J.-P. Piquemal, D. N. Beratan, W. Yang, NCIPLOT: a program for plotting non-covalent interaction regions, J. Chem. Theory Comput. 7 (2011) 625–632, https://doi.org/10.1021/ct100641a.

[44] T. Lu, A comprehensive electron wavefunction analysis toolbox for chemists, Multiwfn, J. Chem. Phys. 161 (2024) 082503, https://doi.org/10.1063/5.0216272.

[45] A.H. Sheikh, A. Farhana, K. Nethaji, N. Baildya, N.R. Madhu, N.A. Choudhury, P. Shanmugam, S. Pathak, A. Banerjee, S. Adhikari, Synthesis, characterization, DFT optimization, and antimicrobial activities of Co(III) and Cd(II) complexes derived from pyridyl Schiff base ligand N-2-(6-methylpyridyl)-2-hydroxy-1-naphthaldimine, J. Coord. Chem. 78 (2025) 1396–1410, https://doi.org/10.1080/00958972.2025.2503939.

[46] S. Nath, V.K. Deb, N. Baildya, S. Roy, W. Kaminsky, A.K. Verma, A. Rahman, A. Mandal, S.D. Kanmazalp, S. Adhikari, I. Saha, Synthesis, structural characterization, theoretical analysis, and cytotoxic evaluation of a hydrazone-based ligand and its Co(II) complex, Inorg. Chem. Commun. 182 (2025) 115384, https://doi.org/10.1016/j.inoche.2025.115384.

[47] L.H. Al-Wahaibi, S.R.S. Gudimetla, O. Blacque, A.A. El-Emam, M.J. Percino, S. Thamotharan, Interplay of weak noncovalent interactions in (E)-4-chloro-N'-(thiophen-2-ylmethylene)benzohydrazide: Insights from Hirshfeld surface, PIXEL energy and QTAIM analyses, J. Mol. Struct. 1315 (2024) 138822, https://doi.org/10.1016/j.molstruc.2024.138822.

[48] C. Jelsch, K. Ejsmont, L. Huder, The enrichment ratio of atomic contacts in crystals, an indicator derived from the Hirshfeld surface analysis, IUCr J 28 (2014) 119–128, https://doi.org/10.1107/S2052252514003327.

[49] V. Meenatchi, K. Muthu, M. Rajasekar, S.P. Meenakshisundaram, Synthesis, structure, spectral, thermal and first-order molecular hyperpolarizability of 4-benzoylpyridine isonicotinyl hydrazone monohydrate single crystals, Spectrochim. Acta Part A Mol. Biomol. Spectrosc. 124 (2014) 423–428, https://doi.org/10.1016/j.saa.2014.01.051.

[50] R.F.W. Bader, Atoms in Molecules: A Quantum Theory, Oxford University Press, USA, 1994.

[51] C. Gatti, Chemical bonding in crystals: new directions, Zeitschrift Für Krist. - Cryst. Mater. 220 (2005) 399–457, https://doi.org/10.1524/zkri.220.5.399.65073.

[52] E. Espinosa, E. Molins, C. Lecomte, Hydrogen bond strengths revealed by topological analyses of experimentally observed electron densities, Chem. Phys. Lett. 285 (1998) 170–173, https://doi.org/10.1016/S0009-2614(98)00036-0.

[53] K. Ramya, R. Shanmugam, P. Mounica, A. Elangovan, G. Arivazhagan, O-H···N, C-H···O, and O-H···π hydrogen bonds between water and 2-methylpyridine, J. Mol. Liq. 429 (2025) 127593, https://doi.org/10.1016/j.molliq.2025.127593.

[54] C.T. Nemes, C.J. Laconsay, J.M. Galbraith, Hydrogen bonding from a valence bond theory perspective: the role of covalency, Phys. Chem. Chem. Phys. 20 (2018) 20963–20969, https://doi.org/10.1039/c8cp03920h.

[55] L.H. Al-Wahaibi, T. Logalakshmi, O. Blacque, H.M. Hassan, M.J. Percino, A.A. El-Emam, S. Thamotharan, Weak noncovalent interactions of 2,4-disubstituted pyrimidine-5-carbonitriles: Insights from quantum chemical calculations, molecular docking, and molecular dynamics simulations, J. Mol. Struct. 1348 (2025) 143504, https://doi.org/10.1016/j.molstruc.2025.143504.

[56] A.A. El-Emam, E. Saveeth Kumar, K. Janani, L.H. Al-Wahaibi, O. Blacque, M.I. El-Awady, N.H. Al-Shaalan, M.J. Percino, S. Thamotharan, Quantitative assessment of the nature of noncovalent interactions in N-substituted-5-(adamantan-1-yl)-1,3,4-

thiadiazole-2-amines: insights from crystallographic and QTAIM analysis, RSC Adv. 10 (2020) 9840–9853, https://doi.org/10.1039/D0RA00733A.

[57] M. Udayakumar, M. Cerón, P. Ceballos, M.J. Percino, S. Thamotharan, Correlation between structural and optical properties of π-conjugated acrylonitrile derivatives: Insights from X-ray, energy frameworks, TD-DFT and charge density analysis, J. Mol. Struct. 1213 (2020) 128174, https://doi.org/10.1016/j.molstruc.2020.128174.

[58] M.J. Percino, M. Udayakumar, M. Cerón, E. Pérez-Gutiérrez, P. Venkatesan, S. Thamotharan, Weak noncovalent interactions in two positional isomers of acrylonitrile derivatives: inputs from PIXEL energy, Hirshfeld surface and QTAIM analyses, Front. Chem. 11 (2023) 1209428, https://doi.org/10.3389/fchem.2023.1209428.